Effects of arsenic incorporation on jarosite dissolution rates and reaction products

Matthew R. Kendall [a], Andrew S. Madden [a,*], Megan E. Elwood Madden [a], Qinhong Hu [b]

[a] *University of Oklahoma, School of Geology and Geophysics, 100 East Boyd St. Rm. 710, Norman, OK 73019, USA*
[b] *University of Texas at Arlington, Department of Earth & Environmental Sciences, 500 Yates Street, Box 19049, Arlington, TX 76019, USA*

Abstract

Batch dissolution experiments were undertaken on synthetic arsenojarosites at pH 2, pH 8, and in ultra-pure water to better understand the influence of As incorporation on the kinetics and reaction products of jarosite dissolution. Incongruent jarosite dissolution was observed in all experiments. Arsenojarosite lacks the pH dependency observed in K-jarosite dissolution, likely the result of surface arsenate–iron complexes preventing protonation at low pH and repelling hydroxyls at high pH. The stronger bonding of arsenate to iron, compared to sulfate to iron, leads to an enrichment of surface layer arsenate–iron complex sites, inhibiting the dissolution of jarosite with time. The secondary reaction products formed during the dissolution of arsenojarosite include maghemite, goethite, and hematite in ultra-pure water, and ferrihydrite in pH 8 Tris buffered solution. Maghemite initially forms and transitions to hematite with time in ultra-pure water, but increasing arsenic concentrations slow this transition. At pH >3.5, arsenic from the dissolution of arsenojarosite adsorbs onto newly formed reaction products. Arsenic also inhibits the formation of goethite and reduces the crystallinity of the observed maghemite reaction products. The coprecipitation of iron oxides with increasing amounts of arsenic results in a change from spherical to "worm-like" aggregate morphology and provides a sink for arsenic released during arsenojarosite dissolution. This study shows that in open systems with a flush of fresh solution, arsenic incorporation in jarosite results in an increase in dissolution rates. In closed systems, however, increasing surface arsenate–iron complexes inhibit further dissolution of the underlying bulk material, causing a reduction in dissolution rates as arsenic incorporation increases.

1. INTRODUCTION

Jarosite-group minerals $[(K, Na, H_3O)Fe_3(SO_4)_2(OH)_6]$ are common alteration and hydrothermal phases, especially within the oxidized zones of sulfide ore bodies (Dutrizac and Jambor, 2000). Depending on aqueous conditions, jarosite forms in the pH range 1–3 (Alpers et al., 1992; Bigham et al., 1996; Savage et al., 2005). Jarosite is also a by-product in the metallurgical industry, where it is precipitated to scavenge excess dissolved Fe, Zn, Cu, As, and Cd from hot acid-leach solutions (Dutrizac and Jambor, 2000). Jarosite has also been observed or detected in acid sulfate soils (Hyashi, 1994), near oceanic fumaroles (Fulignati et al., 2002; Papike et al., 2006), within acidic saline lakes of Australia (Alpers et al., 1992; Benison and Laclair, 2003), and on the surface of Mars (Squyres et al., 2004).

The oxidative weathering of pyrite, or other ferrous sulfides, is essential to the production of acid mine and acid rock drainage (AMD/ARD) conditions (Bigham and Nordstrom, 2000). These minerals also contain trace to almost 50% arsenic (e.g., arsenopyrite and arsenious pyrite, Fuess et al., 1987) that can be released upon weathering. Jarosite has been shown to incorporate arsenic in AMD/ARD environments (Slowey et al., 2007) and in the metallurgical process where jarosite precipitation is used for the

* Corresponding author. Tel.: +1 405 325 5327; fax: +1 405 325 3140.

E-mail addresses: matthew.r.kendall-1@ou.edu (M.R. Kendall), amadden@ou.edu (A.S. Madden), melwood@ou.edu (M.E. Elwood Madden), maxhu@uta.edu (Q. Hu).

long-term disposal of arsenical waste (Savage et al., 2000, 2005; Paktunc and Dutrizac, 2003; Slowey et al., 2007).

Understanding the effects of arsenic on jarosite dissolution rates and mechanisms requires prerequisite knowledge of the jarosite crystal structure. Jarosite belongs to the isostructural jarosite-alunite group and has the general formula of $AB_3(TO_4)_2(OH)_6$ (Papike et al., 2006). The A-site commonly contains monovalent and divalent cations with a coordination number equal to or greater than 9 (Jambor, 1999; Hawthorne et al., 2000), with K^+, Na^+, and H_3O^+ being the dominant A-site ions but Pb^{2+}, Ca^{2+}, and NH_4^+ may also be incorporated (Basciano and Peterson, 2007). The octahedrally coordinated B-site, commonly observed with less than full occupancy, is filled by trivalent Fe^{3+} in the jarosite group and Al^{3+} in the alunite group (Baron and Palmer, 1996). The T-site is tetrahedrally coordinated with S^{6+} being the dominant ion but As^{5+}, P^{5+}, Cr^{6+}, and Se^{6+} have also been observed (Paktunc and Dutrizac, 2003; Savage et al., 2005; Morin and Calas, 2006; Smith et al., 2006a; Basciano and Peterson, 2007). With the variability in composition, charge balancing of the crystal structure is an inherent problem. Kubisz (1970) suggested that protonation of hydroxyl groups to form water molecules could balance the lack of positive charge in the B-site. Parker (1954) noted the presence of excess water in jarosite, as did Hendricks (1937). Using magnetic resonance, Ripmeester et al. (1986) showed that water molecules substitute for hydroxyl groups in alunite. Within the T-site, incorporation of As^{5+} leads to a net negative charge that may be compensated by protonation of the oxyanion (Paktunc and Dutrizac, 2003). Due to the variability in compositions, the alunite supergroup contains more than 40 characterized minerals.

When viewed down the a-axis, the crystal structure of jarosite shows alternating layers of B-site octahedra and T-site tetrahedra (Papike et al., 2006; Electronic Annex, Fig. EA-1). Savage et al. (2005) studied lattice parameter variability in synthetic arsenojarosite and found that the c-axis expands by as much as 0.174 Å with arsenic substitution. An increased substitution of arsenate for sulfate results in a lengthening of the a- and c-axes and likely influences the stability of jarosite (Paktunc and Dutrizac, 2003). Ionic substitutions that alter the unit cell parameters from ideal jarosite have been shown to influence dissolution rates and solubility. Substitution of H_3O^+ and Na^+ in the A-site significantly increases the solubility of jarosite with respect to end-member K-jarosite (Baron and Palmer, 1996), whereas chromate substitution for sulfate decreases the solubility of end-member K-jarosite (Baron and Palmer, 2002).

XANES and X-ray diffraction analyses show that at least 9.9 wt.% AsO_4^{3-} can be structurally incorporated into synthetic jarosite (Paktunc and Dutrizac, 2003). Paktunc and Dutrizac (2003) and Savage et al. (2005) both demonstrated that arsenate is the only arsenic species incorporated in the jarosite structure and that arsenate substitutes for sulfate. The incorporation of arsenic in jarosite (hereafter referred to as arsenojarosite) may have significant environmental implications, should a change in aqueous conditions occur. For example, freshwater influx from heavy rainfall

events or remediation by the addition of limestone will initiate jarosite dissolution.

Jarosite dissolution at moderate to high pH forms nanoscale iron oxide reaction products, often described as $Fe(OH)_3$ precipitates (Gasharova et al., 2005; Smith et al., 2006a,b; Welch et al., 2008) based on the lack of distinct morphological characteristics in SEM/AFM images. Using Mössbauer spectroscopy, SEM, and TEM, Barron et al. (2006) identified hematite, goethite, ferrihydrite, and lepidocrocite as jarosite reaction products in simulated Martian brines. Their work showed that the addition of phosphate, a chemical analog to arsenate, suppressed the formation of goethite. Based on electron diffraction results (TEM), Elwood Madden et al. (2012) found that dissolution products at pH >3.5 include schwertmannite at low temperatures (277 K), hematite, maghemite, ferrihydrite, and minor goethite at room temperature, and hematite with ferrihydrite at high temperatures (323 K).

It is estimated that mine effluents have damaged 19,300 km of streams and 72,000 ha of lakes and reservoirs (Bigham and Nordstrom, 2000). With as many as 500,000 inactive or abandoned mine sites in the United States (Bigham and Nordstrom, 2000), it is important to understand the complex geochemical reactions that may enhance or reduce the effects of AMD/ARD. The purposes of this investigation were to: (1) determine the effects of arsenic incorporation on rates of jarosite dissolution in conditions similar to AMD/ARD sites (pH 2), remediated AMD/ARD sites (pH 8), and conditions during a sudden influx of "fresh" water (ultra-pure water), (2) identify the nanoscale solid products of dissolution, (3) suggest the mechanism(s) by which dissolution is occurring, and (4) determine the fate of arsenic during arsenojarosite dissolution.

For this study, jarosite ($KFe_3(SO_4)_2(OH)_6$) was synthesized with the addition of varying amounts of aqueous arsenate, forming arsenojarosites (($H_3O)_{1-x}$,K_x)Fe_{3-y}(($SO_4)_{2-z}$,($AsO_4)_z$)($OH)_{6-3y}$ ($H_2O)_{3y}$) with a range of arsenate-sulfate substitution. Far-from-equilibrium batch dissolution experiments were conducted to determine short- and longer-term K^+ release, aqueous As concentrations, and jarosite dissolution reaction products. The reaction products and textural evolution of jarosite grains were observed and identified by TEM analyses.

2. MATERIALS AND METHODS

K-jarosite and arsenojarosites were synthesized using previously developed methods (Baron and Palmer, 1996; Driscoll and Leinze, 2005; Savage et al., 2005). 200 mL of ultra-pure water was heated to 95 °C in a 1 L flask at 1 atm. Ferric sulfate hydrate (52 g), potassium hydroxide (11.2 g), and varying amounts of potassium arsenate were then added to the solution, in that order. The mixture was stirred continuously by a magnetic stir bar and held at 95 °C for 4 h. After the 4 h period, the solution was transferred to centrifuge containers and triply rinsed with 10^{-3} N nitric acid for 15 min for AJ0.6 and AJ2.1 and ul-

tra-pure water for AJ3.7. The residual solids were then dried for 24 h at 110 °C.

Each synthetic sample was analyzed on a Rigaku Ultima IV Powder X-ray Diffractometer to verify jarosite formation. The diffractometer used a copper Kα X-ray source operating at 40 kV and 44 mA. Scans were collected from 10 to 65 degrees 2θ, with a step size of 0.02 degrees 2θ, 3 s dwell time, variable slits, 302 mm^2 irradiated area, and sample rotation of 30 rpm. Mineral identification and pattern manipulation were conducted using MDI Jade 9 software.

For chemical analyses, jarosite and arsenojarosite powders were placed onto conductive tape. Energy-Dispersive X-ray Analysis was undertaken using a Cameca SX50 electron probe micro-analyzer (EPMA) equipped with a PGT PRISM 2000 Energy-Dispersive X-ray detector, SAMx NumeriX pulse processor, and run via the SAMx IDFIX program. Operating conditions were 20 kV accelerating voltage, and 10 nA sample current (measured at the Faraday cup). The chemical formulae for synthetic K-jarosite and arsenojarosites were subsequently calculated using the formula presented by Kubisz (1970).

The surface area of each synthetic sample was determined by the N_2 gas adsorption (BET) method (Emmet and Brunauer, 1937). Prior to BET analysis, the samples were outgassed under vacuum at 30 °C for 24 h.

Far-from-equilibrium dissolution experiments were conducted under a range of solution chemistries at room temperature (296 K) to determine jarosite dissolution rates using K^+ as the reaction variable. In each experiment, 200 mL of solution was added to a 250 mL beaker and stirred with a Teflon-coated magnetic stir bar at ∼600 rpm. Once the stirring was underway, the first control sample was collected. Fifteen minutes later, 0.20 ± 0.007 g of jarosite was added to the solution. Reaction duration was determined relative to the time when the jarosite was added. Experiments were replicated a minimum of three times and terminated after 14 days.

In order to prevent addition of K^+ ions to the batch reactors from the pH electrode, the pH of the pre-jarosite solution was determined from a separate aliquot collected immediately prior to the control sample. The pH of the initial (jarosite + solution) slurry was determined by measuring the pH over 1–15 min intervals from an aliquot collected in a fourth replicate experiment. The pH of the slurry was plotted as a function of time and the pH versus time data fit with a linear trend line to determine the initial slurry pH using the y-intercept of the linear fit (Elwood Madden et al., 2012). Final pH was determined by removing an aliquot of the jarosite-solution slurry following the final sampling point.

In ultra-pure water (18.2 MΩ) experiments, the pH was allowed to drift freely. For pH 2 experiments, the solution contained H_2SO_4 and ultra-pure water, while pH 8 experiments consisted of a 0.5 M Tris solution that was adjusted to pH 8 with the addition of 6 N HCl. For dissolution experiments involving the lowest As containing jarosites (K-jarosite and AJ0.6), samples were taken every 10–15 min for the first 2 h. Due to more rapid reaction progress, the higher As containing jarosite (AJ2.1 and AJ3.7) dissolution experiments were sampled every 2–15 min for the first 2 h. Samples were also collected at increasing time intervals for the following 14 days.

Samples of K-jarosite or arsenojarosite suspension were passed through 0.2 μm cellulose acetate syringe filters and refrigerated until analyzed by Atomic Absorbance Spectrophotometry (AAS, Perkin–Elmer AAnalyst 800) or Inductively Coupled Plasma-Mass Spectrometry (ICP-MS, Perkin–Elmer ELAN DRC II). Reported concentrations represent averages of triplicate analyses. Reagent and calibration blanks were included in each analytical session, and randomly selected duplicates were included. For iron and arsenic analysis, all solutions were acidified to 0.1 M (AAS) or 1% (ICP-MS) trace metal grade HNO_3. For flame AAS, aqueous potassium and iron concentrations were determined after optimizing the optical pathway, flame, and nebulizer settings. Ionization was suppressed by the addition of 2000 mg/L NaCl and 0.2 M HNO_3 to all blanks, standards, and samples. Aqueous arsenic concentrations determined by transversely heated graphite furnace AAS (AAnalyst 800) included Mg and Pd nitrate matrix modifiers. Calibration was performed over the linear response range from 1 to 100 μg/L arsenic. The instrument conditions for ICP-MS were as follows: RF power, 1300 W; plasma argon gas flow 15 L/min; nebulizer argon gas flow 0.9 L/min; auxiliary argon gas flow 1.2 L/min; Meinhard Type A quartz nebulizer; platinum sampling and skimmer cones. A standard solution with 5 ppb of In-115, Sc-45, Li-6 and Bi-209 was used as internal standard and introduced online for ICP-MS measurement.

All aqueous concentrations were normalized to the surface area of the K-jarosite or arsenojarosite added in each experiment. Concentrations did not need to be adjusted due to sampling since the slurry was continuously mixed and the jarosite was always suspended in solution; therefore, the ratio of jarosite/water in the beaker remained unchanged during the experiment.

Short-term dissolution rates were calculated using the first 2 h of K^+ concentrations plotted against reaction time, then fit with a second-order polynomial. The derivative of the equation was taken and the initial rate of K^+ release was then determined (Rimstidt and Newcomb, 1993).

Samples for transmission electron microscopy (TEM) were collected by extracting 10 μL of well-stirred suspension by pipette and dropping it onto a Cu grid with support film. Excess solution was wicked away with a wedge of filter paper. TEM images and Selected Area Electron Diffraction (SAED) patterns were collected using a JEOL 2000FX TEM with an accelerating voltage of 200 keV. High-resolution TEM (HRTEM) imaging was performed on a JEOL 2010F with an accelerating voltage of 200 keV. HRTEM images were analyzed with ImageJ and Digital Micrograph. Fast-Fourier Transforms (FFTs) were analyzed with the DiffTools plugin (Mitchell, 2008).

3. RESULTS

3.1. Characterization of synthetic jarosites

The K-jarosite and arsenojarosite synthesis produced 10YR 6/6 (Munsell color) precipitates with no observable change in precipitate color with increased arsenic incorporation. Bulk chemical composition was determined using EPMA for the A-, B- and T-site elements exclusive of H_3O^+ (Table 1). The chemical formulae for synthetic K-jarosite and arsenojarosites, calculated using the formula from Kubisz (1970), are reported in Table 1 and hereafter referred to as K-jarosite, AJ0.6, AJ2.1 and AJ3.7. Kubisz (1970) recommends normalizing the formula based on full T-site occupancy of $SO_4 = 2$ (in this study $SO_4 + AsO_4 = 2$) with any residual charge imbalance compensated by additional OH^-. Paktunc and Dutrizac (2003) found that the incorporation of small amounts of arsenate for sulfate did not create a large charge-balance issue as long as some of the arsenate was protonated to divalent or monovalent species. However, due to the difficulty in properly identifying the location of excess H^+ ions, which are suggested to jump rapidly from OH to OH, SO_4 to SO_4, or AsO_4 to AsO_4 (Paktunc and Dutrizac, 2003), the general chemical formula from Kubisz (1970) was used. All synthetic K-jarosite and arsenojarosite precipitates showed less than full iron occupancy within the B-site. A solid-solution series between H_3O^+ and K^+ occurs in the A-site, with the hydronium content derived from A-site substitutions of $K + Na + H_3O = 1$. The T-site was occupied entirely by SO_4^{2-} in the K-jarosite precipitates whereas the arsenojarosite precipitates also contained 0.6, 2.1, and 3.7 wt.% arsenic.

X-ray diffraction patterns for synthesized K-jarosite and arsenojarosites were compared to the Powder Diffraction File (Electronic Annex, Fig. EA-2). Peaks arising from additional mineral phases were not observed. An increase in d-spacing (peak shift towards lower 2θ) was observed with increasing arsenic incorporation for all peak positions (Fig. 1). Consistent with XRD results, AJ0.0, AJ0.7, and AJ2.1 show no additional phases observed by TEM. For AJ3.7, however, unidentified fine-grained material was observed associated with grain boundaries, likely the result of rinsing. Jarosite grains exhibit rhombohedral (Fig. 2A) to spherical (Fig. 2C) morphology with grain sizes ranging from 0.05 to 3 microns. BET analysis yielded surface areas of 2.2, 0.8, 1.3 and 3.5 m^2/g for K-jarosite, 0.6, 2.1 and 3.7 wt.% arsenic jarosite, respectively.

3.2. Dissolution at pH 2

3.2.1. Solution chemistry and rate calculations

All experiments showed similar trends; a rapid increase in all aqueous concentrations during the first few days of dissolution followed by a decline in release rates thereafter (Fig. 3). Final arsenic concentrations ranged from below detection ($\sim$10 nM) for K-jarosite to 275 µmol L^{-1} m^{-2} for AJ3.7 (Table 2). Values of measured pH remained approximately 2 (Table 3) throughout the duration of the experiment. Time-course evolution of element molar ratios showed that dissolution at pH 2 was incongruent for all solids (Fig. 4). The As:K molar ratio for AJ3.7 was in excess of the congruent As:K ratio, likely due to sorbed arsenic on the initial jarosite synthesis product that was not fully desorbed during the rinsing process. Similar results were also reported by Smith et al. (2006a).

The average initial potassium release log rates (mol m^{-2} s^{-1}) for K-jarosite, AJ0.6, AJ2.1 and AJ3.7 were -8.42 (± 0.031), -9.11 (± 0.50), -8.70 (± 0.17) and -7.79 (± 0.12), respectively (Table 2). The rapid jump in K^+ at the beginning of all experiments (e.g., Fig. 3A, C, E, and G) was excluded in the calculation of rates.

The increased solubility of iron oxides at pH 2 limits iron oxide reaction products from forming and allows for the calculation of jarosite dissolution rates based on iron release. Sulfate also complexes with iron (Sapieszko et al., 1977), further suppressing precipitation of iron oxides. Average short-term initial iron release log rates (mol m^{-2} s^{-1}) for K-jarosite, AJ0.6, AJ2.1 and AJ3.7 were -9.1 (± 0.00), -8.9 (± 0.05), -9.3 (± 0.28), and -8.8 (± 0.06).

Aqueous chemistry was measured in a single replicate out to 14 days. The evolution of pH, surface area, reaction products, and sorption/desorption prevented a meaningful description of 2-week data in terms of dissolution rate. However, the 14 days surface-area normalized values are reported in Table 2. Sample AJ3.7 had the highest surface-area normalized concentration of aqueous arsenic but the lowest concentration of potassium and iron.

3.2.2. TEM of residual solids

As expected based on iron solubility, reaction products were not observed forming on any jarosite surfaces or in bulk solution for all pH 2 dissolution experiments. Due to the relatively large thickness of many jarosite grains, the electron beam only penetrated the outer edge. Even so, an increasing degree of dissolution was observed with time (Fig. 2D–F). After 2 h, grain boundaries are relatively smooth with minor pitting and boundary roughness begin-

Table 1
Bulk chemical composition determined by Electron Probe Micro-Analysis (EPMA) for synthetic K-jarosite and arsenojarosite precipitates. Chemical formulas were calculated using the formula provided by Kubisz (1970).

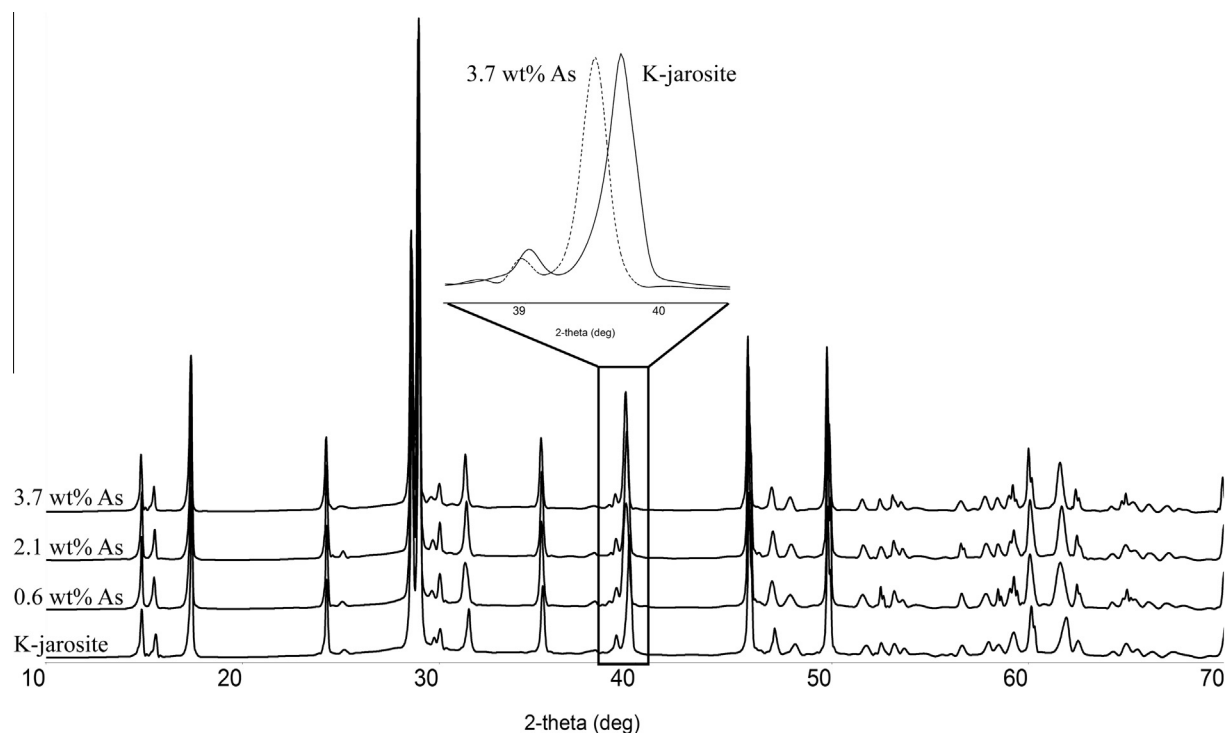| Sample	Bulk chemical composition (wt.%)				Formula of bulk solid based on (S + As) = 2
	K	Fe	S	As	
K-jar	8.79	35.07	15.73	0.00	$(H_3O)_{0.08}K_{0.92}Fe_{2.55}(SO_4)_2(OH)_{4.65}(H_2O)_{1.35}$
AJ0.6	8.36	37.52	14.22	0.61	$(H_3O)_{0.05}K_{0.95}Fe_{2.98}[(SO_4)_{1.98}, (AsO_4)_{.02}](OH)_{5.94}(H_2O)_{0.06}$
AJ2.1	8.64	35.67	14.50	2.10	$(H_3O)_{0.07}K_{0.93}Fe_{2.71}[(SO_4)_{1.90}, (AsO_4)_{.10}](OH)_{5.04}(H_2O)_{0.96}$
AJ3.7	8.56	36.56	12.56	3.70	$(H_3O)_{0.02}K_{0.98}Fe_{2.92}[(SO_4)_{1.80}, (AsO_4)_{.20}](OH)_{5.57}(H_2O)_{0.43}$

Fig. 1. XRD pattern of synthetic K-jarosite and arsenojarosite. A shift in peak positions toward higher *d*-spacing values (lower 2θ region) occur as arsenic incorporation increases.

ning to develop. After 14 days, grain textures showed significant dissolution with all jarosite grains showing some degree of pitting, creating a patchy texture in the thinner jarosite grains (especially Fig. 2D shows this well). SAED patterns of the thinner jarosite grains exhibiting the patchy texture resulted in *d*-spacing values consistent with the original jarosite *d*-spacing values obtained from XRD. The lack of reaction products allowed for the measurement of surface area due to dissolution with AJ0.6 increasing from 0.75 to 2.63 m^2/g after 14 days, and AJ2.1 increasing from 1.27 to 2.44 m^2/g after 14 days.

3.3. Dissolution in ultra-pure water

3.3.1. Solution chemistry

In ultra-pure water, concentrations of As and Fe are significantly lower than these measured from the pH 2 dissolution experiments (Fig. 5). Experiments show similar trends: a rapid increase in K concentrations that then increases more gradually with time, low Fe concentrations that slowly increase or plateau through time, and As concentrations that remain near background levels throughout. Table 3 reports the slurry, initial and final pH values from these experiments. All experiments showed a decrease in pH with reaction progress. The average initial potassium release log rates (mol m^{-2} s^{-1}) for K-jarosite, AJ0.6, AJ2.1 and AJ3.7 in ultra-pure water were −9.20 (±0.05), −9.04 (±0.14), −8.93 (±0.20) and −7.70 (±0.09), respectively (Table 3).

After 14 days, As concentrations ranged from 0.066 (AJ0.6) to 0.420 (AJ2.1) μmol L^{-1} m^{-2} and Fe concentra-

tions ranged from 21 (AJ3.7) to 100 (AJ0.6) μmol L^{-1} m^{-2} (Table 2). The Fe:K molar ratios after 14 days for AJ0.6, AJ2.1 and AJ3.7 were 0.052, 0.083 and 0.058, much lower than the ratios reported for pH 2 dissolution. Incongruent dissolution is inferred based on these values and substantiated with TEM observations of reaction products. Fe:K molar ratios as high as 0.43, 0.48 and 0.12 were observed during the first 2 h of dissolution as Fe was being precipitated out and released more slowly than K. The As:K molar ratios after 14 days were zero (to four decimal places) for all experiments. During the first 2 h of dissolution, the largest As:K ratio observed for any experiment was 0.004.

3.3.2. TEM of residual solids

The solubility of iron oxides in the pH range 4–5 is lower than that of pH 2 and as a result, abundant reaction products were observed from the dissolution of K-jarosite and arsenojarosites in ultra-pure water. The mineralogy of the reaction products evolved with time. For K-jarosite, hematite and maghemite were the dominant phases present after 10 h of dissolution but after 14 days, hematite was dominant with minor goethite and maghemite (Elwood Madden et al., 2012). For AJ0.6, ferrihydrite, hematite, and maghemite were the dominant phases observed after 24 h of dissolution. Transformation to predominantly ferrihydrite and hematite occurred by 14 days with minor goethite (e.g., Electronic Annex, Fig. EA-3A and B). For AJ2.1, ferrihydrite and arsenic-bearing ferrihydrite, described as "FeOAsOH" by Carlson et al. (2002) were the dominant phases after 14 days. In AJ3.7, a poorly crystalline phase
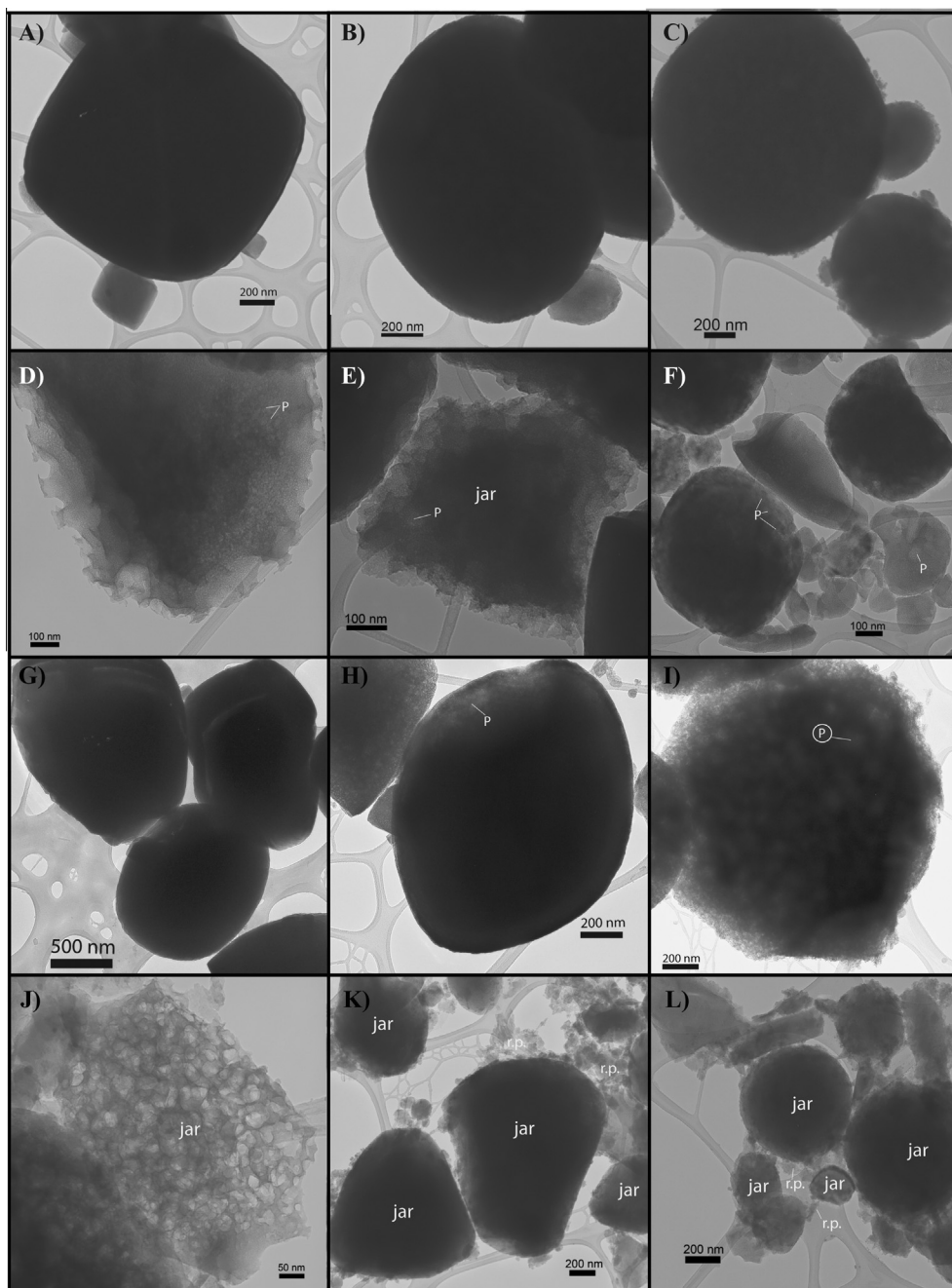
Fig. 2. TEM images of synthesized arsenojarosite starting material for AJ0.6 (A), AJ2.1 (B), and AJ3.7 (C) and reaction products (D–L). In pH 2 H_2SO_4 solution after 2 weeks of dissolution: AJ0.6 (D), AJ2.1 (E) and AJ3.7 (F). AJ0.6 in ultra-pure water after 2.5 h (G), 16.5 h (H), and 2 weeks (I). In pH 8 Tris buffered solution after 2 weeks: AJ0.6 (J), AJ2.1 (K), and AJ3.7 (L). P – pit, jar – jarosite, r.p. – reaction product.

was observed throughout the entire 14 days, eventually after 2 weeks appearing as "FeOHAs".

In K-jarosite dissolution experiments with ultra-pure water, Elwood Madden et al. (2012) reported subhedral maghemite grains with sizes between 10–50 nm. With time, hematite of 5–10 nm rounded to subhedral grains, or ~50 nm subhedral to euhedral grains with varying morphologies, became dominant (Elwood Madden et al.,

2012). For AJ0.6 experiments, reaction products occurred as aggregates of 5–10 nm subhedral grains or within aggregates containing goethite where the individual grains could not be identified (Fig. 6A). In AJ2.1 and AJ3.7 experiments, the reaction products occurred predominantly associated with jarosite grains and exhibited a "worm-like" (Fig. 6C and D) aggregate morphology. Crystal domains, however, still consisted of 5–10 nm subhedral grains.
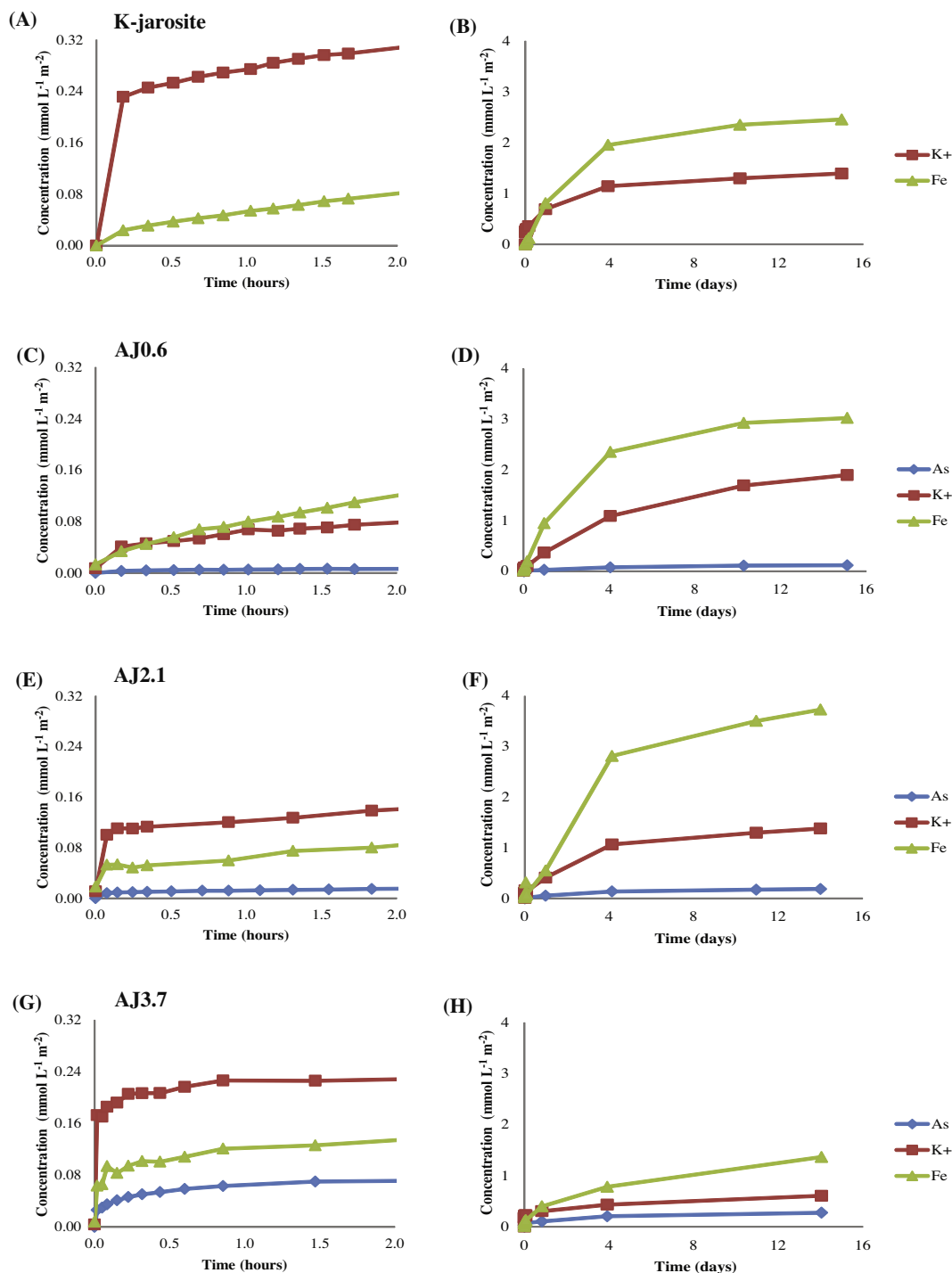
Fig. 3. Elemental concentrations from the dissolution of AJ0.0 (A and B), AJ0.6 (C and D), AJ2.1 (E and F) and AJ3.7 (G and H) in pH 2 H_2SO_4 solution.

Reaction products from K-jarosite, AJ0.6, and AJ2.1 were crystalline, whereas reaction products from AJ3.7 experiments exhibited a poorly crystalline phase throughout. After 14 days, HRTEM images of AJ0.6 and AJ2.1 reaction products (Fig. 6A–B and D–E) showed abundant lattice and Moiré fringes, whereas poorly crystalline AJ3.7 reaction products showed no measureable lattice fringes (Fig. 6G and H). The spots in FFTs of HRTEM images (Fig. 6C, F, and I) provide a reciprocal space depiction of the distribution of these fringes. The spacings should not be over-interpreted, since they depend on the angle of overlap for overlying crystals and the exact focal conditions, which were set for best contrast rather than measurement. However, the lack of spots in the AJ3.7 FFT (Fig. 6I)

Table 2
Aqueous concentrations after 14 days normalized for initial surface area.

Sample	K mmol L^{-1} m^{-2}	Fe mmol L^{-1} m^{-2}	As µmol L^{-1} m^{-2}
pH 2			
AJ0.6	1.90	3.03	118
AJ2.1	1.38	3.73	188
AJ3.7	0.230	0.126	275
UP water			
AJ0.6	1.91	0.100	0.066
AJ2.1	0.969	0.080	0.420
AJ3.7	0.368	0.021	0.119
pH 8			
AJ0.6	1.70	0.230	3.28
AJ2.1	1.18	0.252	19.0
AJ3.7	0.418	0.135	20.2

is typical of the lack of fringes in reaction product HRTEM images. The Energy-Dispersive X-ray Spectroscopy (EDS) of the 14 days reaction products showed an increase in the amount of arsenic associated with the reaction products of AJ3.7 compared to AJ0.6 reaction products. Overall, alteration of aggregate morphology from spherical to "worm-like" segments and decreased particle crystallinity were observed with increased arsenic concentrations.

All jarosite grain textures indicated an increased degree of dissolution with time (e.g., Fig. 2G–I). Reaction products were heavily associated with K-jarosite and arsenojarosite grains and often obscured direct observations of the grain boundaries. After 2 h, grain boundaries were relatively smooth with minor pitting and boundary roughness beginning to develop. After 14 days, abundant reaction products were observed associated with jarosite grain boundaries, but jarosite grains exhibited pitting (Fig. 2I) and surface roughness where reaction products were not observed.

3.4. Dissolution at pH 8

3.4.1. Solution chemistry

Within the first 2 h of reaction at pH 8 (Tris buffered), concentrations of As and Fe were significantly lower than

Table 3
Solution conditions and dissolution rates for K-jarosite and arsenojarosite experiments in this study.

| Sample	Condition	Slurry pH	Initial pH	Final pH	Rate (mol m^{-2} s^{-1})	Log r
K-jar	H_2SO_4	2.0	2.0	2.0	3.60×10^{-9}	−8.44
K-jar	H_2SO_4	2.0	2.0	2.0	3.61×10^{-9}	−8.44
K-jar	H_2SO_4	2.0	2.0	2.0	4.08×10^{-9}	−8.39
AJ0.6	H_2SO_4	2.0	2.1	2.0	6.56×10^{-10}	−9.18
AJ0.6	H_2SO_4	2.0	2.1	2.0	2.63×10^{-9}	−8.58
AJ0.6	H_2SO_4	2.0	2.1	2.0	2.64×10^{-10}	−9.58
AJ2.1	H_2SO_4	2.0	2.1	2.0	1.57×10^{-9}	−8.80
AJ2.1	H_2SO_4	2.0	2.1	2.0	3.13×10^{-9}	−8.50
AJ2.1	H_2SO_4	2.0	2.1	2.0	1.57×10^{-9}	−8.80
AJ3.7	H_2SO_4	2.0	2.0	2.0	2.23×10^{-8}	−7.65
AJ3.7	H_2SO_4	2.0	2.0	2.0	1.39×10^{-8}	−7.86
AJ3.7	H_2SO_4	2.0	2.0	2.0	1.39×10^{-8}	−7.85
AJ0.6	Water	4.9	5.5	4.8	1.27×10^{-9}	−8.90
AJ0.6	Water	4.9	5.5	4.8	6.58×10^{-10}	−9.18
AJ0.6	Water	4.9	5.5	4.8	9.23×10^{-10}	−9.03
AJ2.1	Water	5.4	5.7	5.1	6.95×10^{-10}	−9.16
AJ2.1	Water	5.4	5.7	5.1	1.55×10^{-9}	−8.81
AJ2.1	Water	5.4	5.7	5.1	1.55×10^{-9}	−8.81
AJ3.7	Water	4.1	5.7	3.9	1.93×10^{-8}	−7.72
AJ3.7	Water	4.1	5.7	3.9	1.68×10^{-8}	−7.78
AJ3.7	Water	4.1	5.7	3.9	2.49×10^{-8}	−7.60
AJ0.6	Tris	7.6	8.0	8.0	1.33×10^{-9}	−8.88
AJ0.6	Tris	7.6	8.0	8.0	6.63×10^{-10}	−9.18
AJ0.6	Tris	7.6	8.0	8.0	1.07×10^{-9}	−8.97
AJ2.1	Tris	7.7	7.7	7.9	4.72×10^{-10}	−9.33
AJ2.1	Tris	7.7	7.7	7.9	2.35×10^{-10}	−9.63
AJ2.1	Tris	7.7	7.7	7.9	3.94×10^{-10}	−9.40
AJ3.7	Tris	7.9	8.0	8.0	8.45×10^{-9}	−8.07
AJ3.7	Tris	7.9	8.0	8.0	1.13×10^{-8}	−7.95
AJ3.7	Tris	7.9	8.0	8.0	2.81×10^{-8}	−7.55
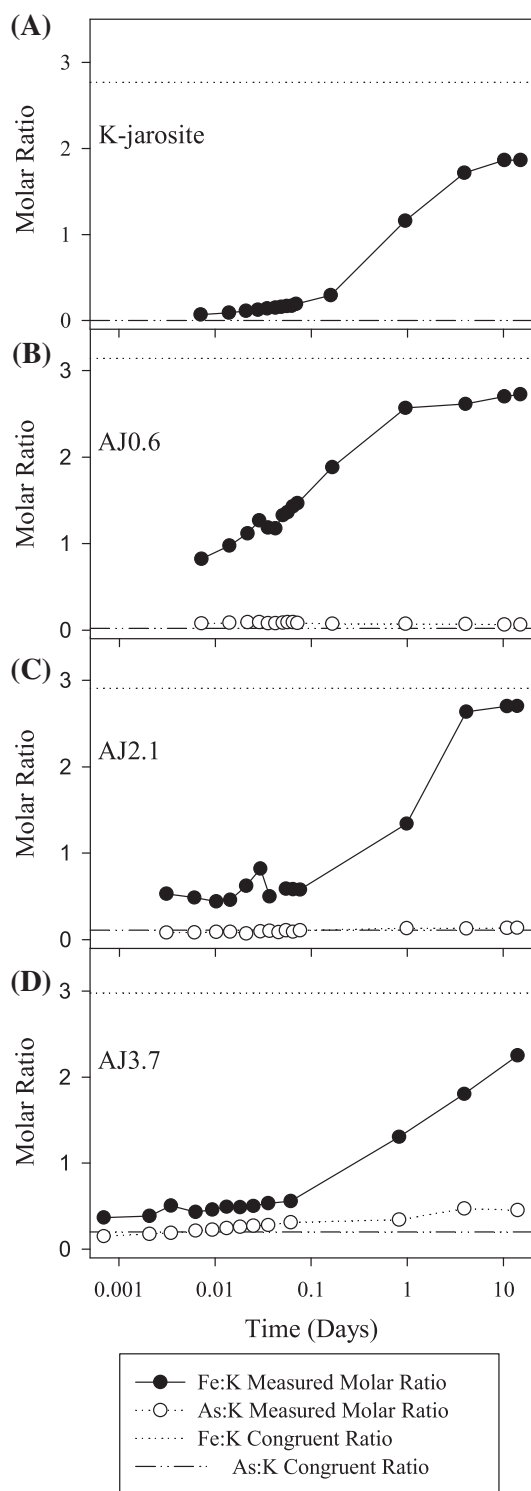
Fig. 4. Time-course evolution of element molar ratios (Fe:K and As:K) during dissolution of K-jarosite and arsenojarosite in pH 2 H_2SO_4 solution. All samples dissolve incongruently during the duration of the dissolution experiments. The measured As:K molar ratio for AJ3.7(D) is in excess of the expected congruent molar ratio, likely due to excess arsenic adsorbed on the jarosite that was not thoroughly desorbed during the rinsing procedure prior to the dissolution experiments.

As and Fe concentrations from the pH 2 dissolution experiments and only slightly lower than concentrations from the ultra-pure water dissolution experiments (Fig. 7, as compared with Figs. 3 and 5). After several days of dissolution, reacted jarosite particles and reaction products passed through the 0.2 μm filter (Electronic Annex, Fig. EA-4), leading to the observed increase in aqueous concentrations. A control experiment with AJ0.6 demonstrated no jarosite could be detected by TEM passing the filters during the period of data collection used to calculate dissolution rates. All pH 8 experiments showed similar trends; an initial rapid in-
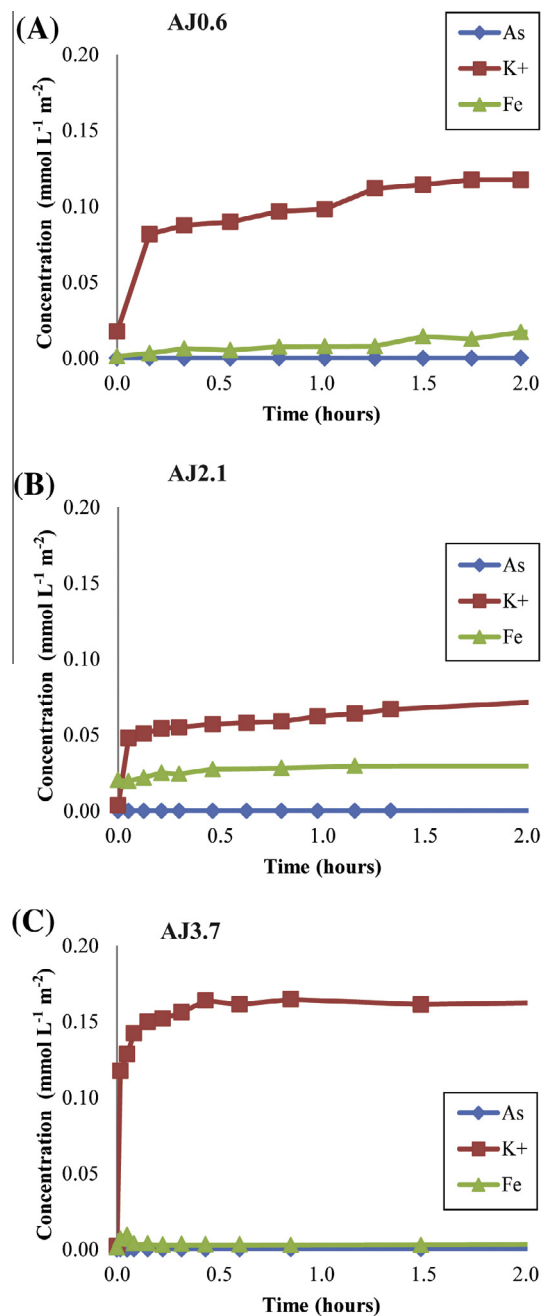

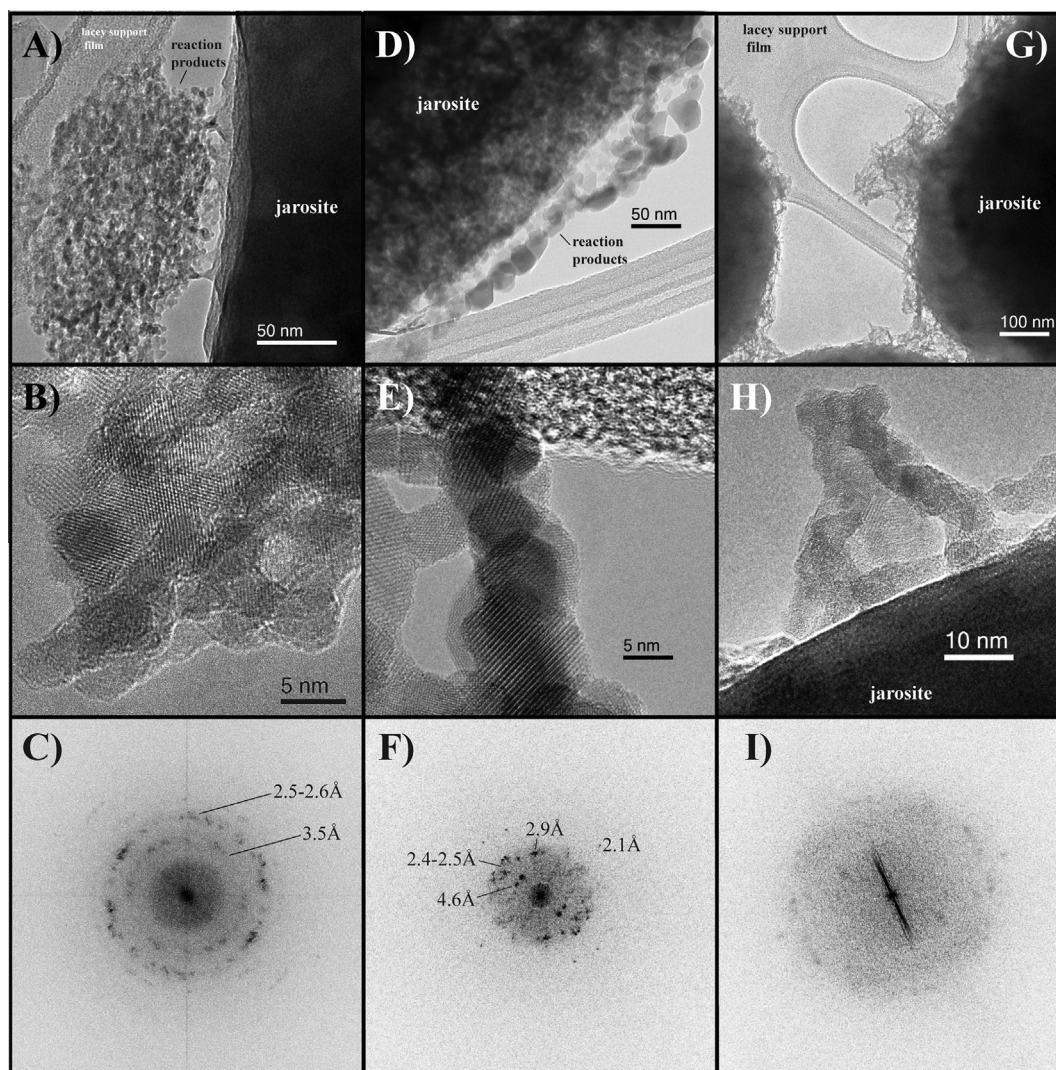Fig. 5. As, K, and Fe released during dissolution of AJ0.6 (A), AJ2.1 (B) and AJ3.7 (C) in ultra-pure water.

Fig. 6. TEM/HRTEM images and FFTs of reaction products from the dissolution of AJ0.6 (A–C), AJ2.1 (D–F), and AJ3.7 (G–I) in ultra-pure water. A change in aggregate morphology and particle crystallinity occur with increased arsenic concentration, as verified by FFTs (shown) and EDS (not shown).

crease in K concentrations in the first few hours, followed by a steadily declining rate with time, low Fe concentrations that slowly increased through time, and As concentrations that remained low but increased steadily as the experiment progressed. The pH remained approximately 8 throughout all experiments (Table 3). The average short-term initial potassium release log rate (mol m^{-2} s^{-1}) for K-Jarosite, AJ0.6, AJ2.1 and AJ3.7 were -7.95 (±0.13), -9.01 (±0.15), -9.45 (±0.16) and -7.86 (±0.27), respectively (Table 2).

After 14 days, As concentrations ranged from 3.28 (AJ0.6) to 20.2 (AJ3.7) μmol L^{-1} m^{-2} with Fe concentrations ranging from 135 (AJ3.7) to 252 (AJ2.1) μmol L^{-1} m^{-2} (Table 2). The lowest concentration of surface-area normalized K$^+$ was again found in experiments with AJ3.7. At pH 8, the solubility of iron oxides are at a minimum. However, after 14 days the Fe:K molar ratios for AJ0.6, AJ2.1 and AJ3.7 were 0.13, 0.21 and 0.32, higher than the ratios reported during dissolution in ultra-pure water at pH 4–5, likely a result of material passing through the filter. Incongruent dissolution is inferred based on molar ratio values and substantiated with TEM observations of reaction products. Fe:K molar ratios steadily increased as the experiment progressed. The final (14 days) As:K molar ratios for AJ0.6, AJ2.1 and AJ3.7 were 0.002, 0.016, and 0.048, respectively.

3.4.2. TEM of residual solids

Abundant reaction products formed on K-jarosite and arsenojarosite surfaces and in bulk solution for all TEM sampling times (e.g., Figs. 2K and L, and EA-3H–L). Reaction product identification was difficult due to a film remaining over much of the residual solids on the TEM grids. This film was likely the result of the Tris buffered solution, since pH 2 and ultra-pure water samples did not contain this film. Areas on every grid remained unobscured.
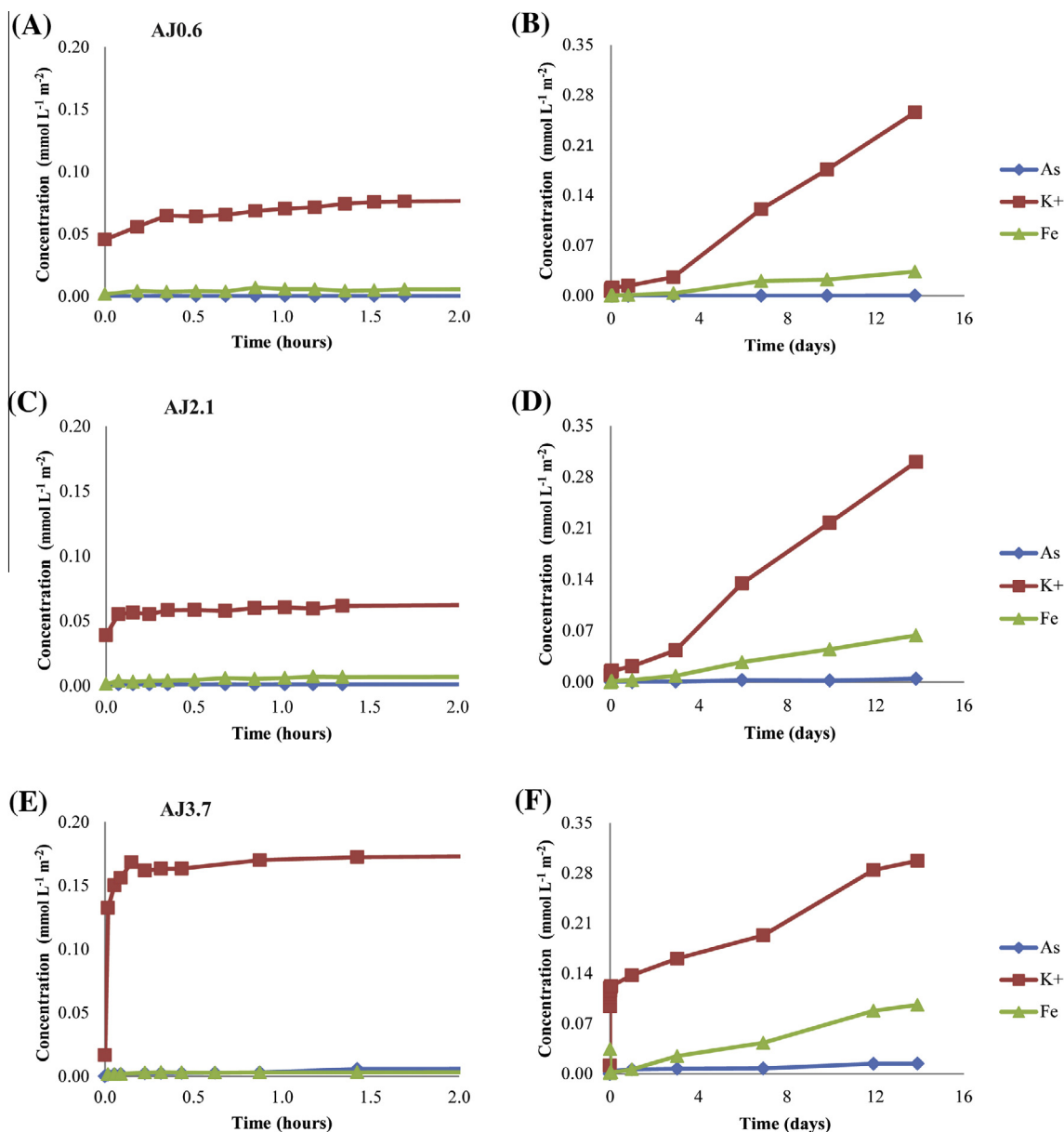
Fig. 7. Elemental concentrations from the dissolution of AJ0.6 (A and B), AJ2.1 (C and D) and AJ3.7 (E and F) in pH 8 TRIS buffered solutions. The increase in all concentrations after several days of dissolution is the results of jarosite and colloidal material passing through the 0.2 μm filter.

In these film-free areas, abundant poorly crystalline material provided no discernible electron diffraction pattern. Aggregates of ~5 nm ferrihydrite were predominant phase identified along with minor hematite and maghemite (Fig. EA-3H–L).

The evolution of jarosite grain textures showed an increasing degree of dissolution with time. After 2 h, grain boundaries had minor pitting and boundary roughness. After 14 days, dissolution textures were pervasive. All jarosite grains showed some degree of pitting, creating a patchy texture in the thinner jarosite grains (Fig. 2J). SAED patterns of the thinner patchy jarosite grains gave *d*-spacing values consistent with the original jarosite *d*-spacing values obtained from XRD.

4. DISCUSSION

4.1. Dissolution rates

The dissolution rates measured in this study are similar to rates calculated from synthetic K-jarosite dissolution data presented in the literature (Baron and Palmer, 1996; Smith et al., 2006b; Elwood Madden et al., 2012). However, dissolution rates for K-jarosite containing substitutions in the T-site are presented here for the first time. Examples of jarosite dissolution experiments in the literature where T-site substitutions either occurred or possibly occurred include Smith et al. (2006a) and Welch et al. (2007). Smith et al. (2006a) conducted dissolution experiments on Pb-

Table 4
Reported corresponding solution conditions and K-jarosite dissolution rates from other studies.

Source	Condition	Slurry pH	Initial pH	Final pH	Rate ($mol\,m^{-2}\,s^{-1}$)	Log r
Elwood Madden et al. (2012)	H_2SO_4	2.0	2.0	1.7	3.24×10^{-9}	−8.49
Elwood Madden et al. (2012)	H_2SO_4	2.0	2.1	1.6	2.82×10^{-9}	−8.55
Elwood Madden et al. (2012)	H_2SO_4	2.0	2.0	1.7	2.51×10^{-9}	−8.6
Elwood Madden et al. (2012)	Water	4.4	7.1	4.4	7.08×10^{-10}	−9.15
Elwood Madden et al. (2012)	Water	4.4	6.9	4.3	6.03×10^{-10}	−9.22
Elwood Madden et al. (2012)	Water	4.4	6.5	4.4	5.75×10^{-10}	−9.24
Elwood Madden et al. (2012)	MES	7.5	7.9	6.7	8.31×10^{-9}	−8.08
Elwood Madden et al. (2012)	MES	7.5	8.1	6.8	1.10×10^{-8}	−7.96
Elwood Madden et al. (2012)	MES	7.5	8.0		1.51×10^{-8}	−7.82
Smith et al. (2006b) (first 85 days)	HCl		2.0			−8.8
Smith et al. (2006b) (first 85 days)	CaOH		8.0			−9.1
Welch et al. (2008)	Water		3.8			−11.2 (0.1)
Welch et al. (2008)	HCl		4.0			−11.3 (0.9)
Welch et al. (2008)	HCl		3.0			−11.4 (0.4)
Welch et al. (2008)	H_2SO_4		4.0			−11.3 (0.5)
Welch et al. (2008)	H_2SO_4		3.0			−11.8 (0.3)
Gasharova et al. (2005)	Water		5.5			−6.8 (0.4)
Baron and Palmer (1996)	HCl		2.0			−8.5 (0.03)

and Pb–As-jarosites, but dissolution rates could not be calculated due to the chemical behavior of Pb^{2+}. Pb^{2+} substitutes for K^+ in the A-site but precipitated out with sulfate during the dissolution of Pb–As-jarosite at pH 2 and 8. Welch et al. (2007) collected dissolution data on a natural jarosite sample where chromate, which readily substitutes into the T-site, was observed associated with jarosite. However, Welch et al. (2007) noted that it was impossible to determine if the elements originated from the A-, B-, or T-site or if they were associated with another phase and/or sorbed to surfaces.

Due to the lack of K-jarosite dissolution experiments with known T-site substitutions, dissolution rates from this study are compared solely with rates calculated from K-jarosite without T-site substitutions. When comparing rates from this study with dissolution data in the literature (Tables 3 and 4), there was a difference in the time scale over which the dissolution rates were calculated. Initial dissolution rates calculated for this study are based on data collected during the first 2 h of dissolution (short-term), whereas data from Welch et al. (2007), Smith et al. (2006b), and Baron and Palmer (1996) were collected over a much greater time span (12–166 days). K-jarosite dissolution rates to date (Table 4) were compiled and critically evaluated by Elwood Madden et al. (2012). Rates calculated in pH 2 conditions from the first 85 days of Smith et al. (2006b) data and all of Baron and Palmer (1996) data show similar rates to short-term rates calculated for K-jarosite, AJ0.6, and AJ2.1 at pH 2 in this study. Calculated AJ3.7 short-term rates are substantially faster than all the rates reported in the literature.

4.2. Dissolution mechanisms

The average short-term dissolution rates calculated for arsenojarosite generally increase as the amount of incorporated arsenic increases, with the exception of AJ2.1 at pH 8 (Fig. 8). This observed increase in dissolution rates is likely a result of the instability within the jarosite structure due to the incorporation of the slightly larger and higher charged arsenate complex which polarizes the surrounding bonds, making them more susceptible to attack. A possible explanation for the anomalous behavior of AJ2.1 is the greater number of iron vacancies in this sample (Table 1) may accommodate strain from arsenic substitution. However, this stabilization would be expected to slow rates at all pH values. Similar dissolution rates observed at all three solution conditions for AJ0.6 and AJ3.7 and their similar bulk solid K, Fe, and hydroxyl/water stoichiometry indicate that the dissolution rate may also be related to the stoichiometry in the A-site, B-site, or hydroxyl/water site.

K-jarosite exhibits a substantial variation in dissolution rates for the different solution conditions (Fig. 9). Elwood Madden et al. (2012) showed that K-jarosite dissolution is dependent on pH with a minimum rate occurring at pH ~3.5. Two different dissolution mechanisms were suggested to be occurring; at pH <3.5, H^+ attack is the dominant mechanism while at pH >3.5, OH^- attack is the controlling mechanism. Arsenojarosite dissolution rates presented here suggest that a third mechanism may also play a role near the point of zero charge of K-jarosite, where dissolution would be controlled by H_2O attack. Similar trends have been observed in the pH-dependence of dissolution rates for many minerals (e.g., Brady and House, 1996; Brantley, 2008).

The pH-dependence of arsenojarosite results are compared with the pH-dependent rate of K-jarosite dissolution determined by Elwood Madden et al. (2012) in Fig. 9. Incorporation of arsenic in jarosite appears to suppress pH dependency, with AJ0.6 and AJ3.7 having nearly constant log r of −9.0 and −7.7, respectively, through all pH values and AJ2.1 having a slightly decreasing log r from −8.8 to −9.4 as pH increases from 2 to 8. We suggest that the incorporation of arsenic into jarosite limits the effective-
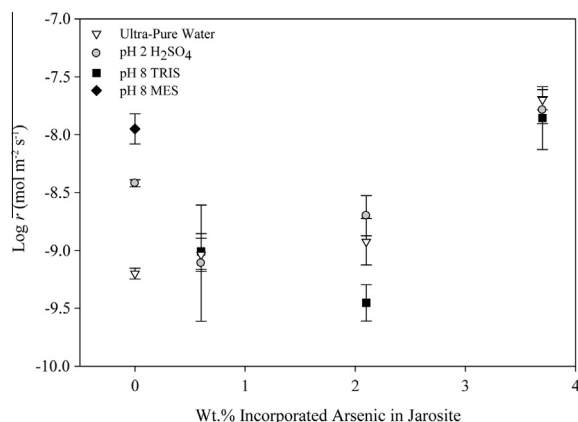
Fig. 8. Dissolution rates of K-jarosite and arsenojarosite versus concentration of incorporated arsenic. In general, dissolution rates increase as the amount of incorporated arsenic increases.
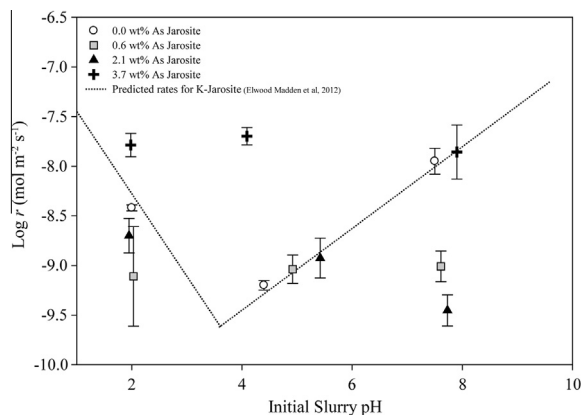

Fig. 9. Dissolution rates of K-jarosite and arsenojarosite versus slurry pH at room temperature. Dotted line represents predicted rates for K-jarosite dissolution from Elwood Madden et al. (2012). Errors bars represent one standard deviation from replicate experiments.

ness of H^+ and OH^- attack, resulting in a predominantly H_2O attack mechanism in arsenojarosite. This change in mechanism may be due to surface-bound arsenate preventing protonation at low pH and creating electrostatic repulsion of hydroxyls at higher pH.

The preferential removal of K^+ and SO_4^{2-} during dissolution (e.g., Fig. 4) reveals an underlying layer of Fe–OH–Fe octahedra where the differences in bonding behavior between arsenate and sulfate become evident. Sulfate associates relatively weakly with ferric iron, while arsenate forms strong ligand-exchange complexes. Therefore, sulfate is preferentially released to solution versus arsenate. Pauling ionic bond-valence analysis of oxygen atoms surrounding a hypothetical iron site in stoichiometric jarosite illustrates that the dissolution of jarosite is likely controlled by the breaking of Fe–O bonds (Elwood Madden et al., 2012). Since the breaking of Fe–OH bonds is likely the rate limiting step in jarosite dissolution, the removal of K^+ and SO_4^{2-} during dissolution results in an accumulation of

arsenate at Fe–OH sites that prevents further attack by H^+ and OH^- in solution. It may be that the location of the minimum in the dissolution rate of K-jarosite (i.e., the point of the "V" in Fig. 9) near pH 3.5, and thus the change in mechanism, relates to the hydrolysis of surface-associated Fe.

Based on the observation of incongruent dissolution, we infer the rates of mineral dissolution are related in a complex manner to the distribution of surface functional groups (e.g., Brantley, 2008), but the aqueous data (e.g., Fig. 4) suggest this distribution evolves with time. Modeling of arsenate adsorption and surface speciation on goethite and iron oxides by Fukushi and Sverjensky (2007) suggested that the most stable arsenate–iron surface complexes are $(>FeO)_2AsOOH$ at pH <5 and $(>FeO)_2AsO_2^-$ at pH >5. For arsenojarosite, we hypothesize that arsenate–iron surface complexes limit the effectiveness of H^+ and OH^- attack on the Fe–OH bonds, affect iron hydrolysis, and instead cause the overall short-term dissolution rate to be controlled by the attack of H_2O on the Fe–OH bonds.

The surface area-normalized concentration of K^+ in solution at 14 days of dissolution decreases for all experiments as arsenic incorporation increases, providing supporting evidence for a conceptual model wherein residual arsenate surface complexes slow further dissolution, (Fig. 10). It would be expected that a faster initial dissolution rate (Table 3, Fig. 8) with increased arsenic incorporation would create a greater concentration of K^+ in solution after 14 days, but the opposite trend was observed in this study.

In general, adsorption of inorganic oxyanions (e.g., phosphate, borate, and arsenate) that form bidentate binuclear surface complexes on oxide minerals leads to a decrease in dissolution rate (Stumm, 1997). For example, phosphate-loaded goethite dissolved much more slowly in HCl than phosphate-free goethite (Strauss et al., 1997). Eick et al. (1999) demonstrated that arsenate adsorbed on the surface of goethite inhibited oxalate promoted dissolution, except at pH 6. Arsenate was more efficient at competing for goethite surface sites than oxalate and subsequently increased the negative charge of the surface. This reduced the rates of water exchange around iron, thereby decreasing
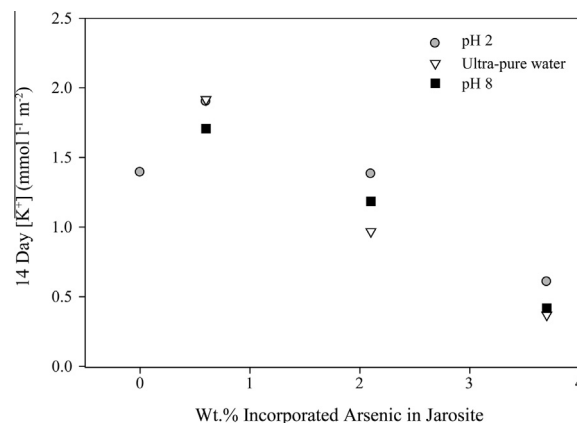

Fig. 10. Concentration of K^+ in solution after 14 days of dissolution decreases as the amount of incorporated arsenic increases.

the dissolution rates (Eick et al., 1999). Decades of research have demonstrated a direct link between metal–ligand complexation and water exchange rates (e.g., Rustad and Casey, 2012). Stumm (1997) also suggested that the release or removal of such complexes is energetically unfavorable, inhibiting proton- or ligand (hydroxyl)-promoted dissolution.

4.3. Residual solids

The residual solids produced during jarosite dissolution were volumetrically dominated by reacted jarosite grains at all sampling periods. Secondary reaction products become more abundant with time, especially at 14 days in pH >3.5 experiments. These reaction products were only apparent from TEM observations, as other techniques (e.g., XRD and SEM) were incapable of resolving and identifying the nanoscale reaction products.

The secondary reaction products observed during the dissolution of K-jarosite and arsenojarosite varied as a function of time, pH, and arsenic concentration, as identified by SAED. HRTEM images were also acquired, showing a multitude of lattice fringes (Fig. 6B and D) for many of the reaction products when the amount of incorporated arsenic was 2.1% or less. On the other hand, selected-area electron diffraction patterns were less likely to indicate crystallinity; patterns for many AJ0.6 and AJ2.1 reaction products were dominated by broad rings with a smaller number of spots. This is typical for phases such as "2-line" ferrihydrite, where lattice fringes are common even as SAED and XRD patterns are diffuse (e.g., Janney et al., 2000).

On the other hand, increasing arsenic load leads to a decrease in reaction product crystallinity. This is significant because, for example, amorphous ferric arsenate leads to arsenic solubilities greater than typical regulatory thresholds (e.g., Paktunc and Bruggemann, 2010). A reduction in crystallinity has also been observed by Waychunas et al. (1993) and Violante et al. (2007) for arsenate coprecipitated with iron oxides and Galvez et al. (1999) for ferrihydrite coprecipitated with phosphate. Additionally, at pH 8, ferrihydrite solubility is very low, preventing recrystallization of the initial reaction product to form more thermodynamically stable phases. We hypothesize that the observed change in aggregate morphology from spherical (Fig. 6A) to "worm-like" (Fig. 6D, E, G, and H) can be attributed to repulsive forces created by the increase in negative charge of the particles as arsenic association increases, limiting the surface interactions of particles.

5. IMPLICATIONS

Iron oxides have important implications on the fate and transport of arsenic in AMD/ARD environments (Cheng et al., 2009) as many have points of zero charge at pH $\sim$8.5 (pH$_{pzc}$, pH at which the net surface charge is zero). As previously discussed, the dominant aqueous arsenate species present at surface water conditions (pH 4–9) are $H_2AsO_4^-$ and $HAsO_4^{2-}$ which readily adsorb to the surface of the positively charged iron oxy(hydr)oxides. In extremely acidic (pH <2) or alkaline (pH >9.5) environments, arse-

nate will be released through desorption from or dissolution of the parent iron oxide. However, within the pH range of common surface waters the adsorption of arsenate on iron oxides can be beneficial in mitigating arsenic migration (Cheng et al., 2009). The ultra-pure water and pH 8 solutions used in this study for the dissolution of arsenojarosite favor the precipitation of iron oxides that serve as a sink for arsenic. The element concentration profiles from these experiments (Figs. 5 and 7) show a net deficiency of arsenic and iron in solution compared to the pH 2 dissolution experiment (Fig. 3). Fe:K and As:K molar ratios also indicate a net deficiency of these two elements in solution. TEM observations of iron oxide precipitation explain the low but measurable iron concentrations and low Fe:K molar ratios. The low aqueous arsenic concentration and low As:K molar ratio that follow similar trends as iron, suggest that a portion of the aqueous arsenic has adsorbed onto and/or coprecipitated with the newly formed iron oxide nanoparticles, also verified by EDS. Subsequently, the release of arsenic from arsenojarosite dissolution and the rapid adsorption of arsenic by newly formed iron oxides show that the mobility of arsenic in AMD/ARD systems is dependent on the cycling of arsenic on or within several minerals. Jarosite has the capability to serve as a sink for arsenic in highly acidic environments whereas iron oxides serve as an additional sink for arsenic in conditions that are unfavorable for jarosite (pH >3–4).

The direct effects of arsenic incorporation on the dissolution kinetics of jarosite have not been previously investigated. The experimental data from this study suggest that the dissolution kinetics of arsenojarosite differs profoundly from that of K-jarosite in terms of dissolution rates and mechanisms. In open systems (e.g., most AMD/ARD systems), the increase in initial dissolution rates may lead to a sudden influx of arsenic that could detrimentally affect the ecosystem of the downstream environment upon dissolution.

The batch reactor set-up used in this experiment is a closed system and is representative of conditions in capped AMD/ARD environments and also those thought to have been present on the surface of Mars during aqueous diagenesis of jarosite-bearing deposits. As jarosite dissolution progresses, K^+ and SO_4^{2-} are preferentially leached from the surface (Smith et al., 2006b), forming a residual surface layer of iron. The breaking of Fe–OH bonds is assumed to be the rate-limiting step in jarosite dissolution, but during arsenojarosite dissolution, arsenate likely remains bonded to the surface due to the much stronger bonding nature of arsenate to iron, compared with sulfate to iron. The increased number of arsenate–iron sites also inhibits dissolution in these systems. This study has implications on the calculation of jarosite lifetimes on the surface of Mars (Elwood Madden et al., 2009) due to the reduction in dissolution rates when phosphate, which is chemically similar to arsenate and has been widely observed with jarosite on Mars (Rieder et al., 2004) is incorporated into the jarosite or is present in solution during the dissolution of jarosite. In addition, this study will add to the understanding of the geochemically complex nature of AMD/ARD systems and the potential influence trace elements have on

the dissolution kinetics of minerals present in these environments.

This study also shows that secondary reaction products formed during the dissolution of K-jarosite and arsenojarosite are both kinetically and thermodynamically controlled, similar to results obtained by Elwood Madden et al. (2012). In addition, the presence of arsenate during iron oxide formation alters the mineralogy, crystallinity, and aggregate morphology of the iron precipitates. The transport of arsenic from AMD/ARD environments is, at least in some cases, primarily associated with iron-rich nanoparticles. Our study has shown a concentration increase of arsenic associated with nanosscale crystalline and poorly crystalline reaction products formed during the dissolution of arsenojarosite in ultra-pure water (pH 3.5–5). Arsenate forms inner sphere adsorption complexes with these iron precipitates (Fendorf et al., 1997; Raven et al., 1998; Jain and Loeppert, 2000; Fukushi and Sverjensky, 2007; Slowey et al., 2007) which would allow the arsenic to be transported through rapidly changing geochemical conditions more readily, a common occurrence in AMD/ARD environments (Cheng et al., 2009).

APPENDIX A. SUPPLEMENTARY DATA

Supplementary data associated with this article can be found, in the online version, at http://dx.doi.org/10.1016/j.gca.2013.02.019.

REFERENCES

Alpers C. N., Rye R. O., Nordstrom D. K., White L. D. and King B. S. (1992) Chemical, crystallographic and stable isotopic properties of alunite and jarosite from acid-hypersaline Australian lakes. *Chem. Geol.* **96**, 203–226.

Baron D. and Palmer C. D. (1996) Solubility of jarosite at 4–35 °C. *Geochim. Cosmochim. Acta* **60**, 185–195.

Baron D. and Palmer C. D. (2002) Solid-solution aqueous-solution reactions between jarosite $(KFe_3(SO_4)_2(OH)_6)$ and its chromate analog. *Geochim. Cosmochim. Acta* **66**, 2841–2853.

Barron V., Torrent J. and Greenwood J. P. (2006) Transformation of jarosite to hematite in simulated Martian brines. *Earth Planet. Sci. Lett.* **251**, 380–385.

Basciano L. C. and Peterson R. C. (2007) Jarosite-hydronium jarosite solid-solution series with full iron site occupancy: mineralogy and crystal chemistry. *Am. Mineral.* **92**, 1464–1473.

Benison K. C. and Laclair D. A. (2003) Modern and ancient extremely acid saline deposits: terrestrial analogs for Martian environments? *Astrobiology* **3**, 609–618.

Bigham J. M. and Nordstrom D. K. (2000) Iron and aluminum hydroxysulfates from acid sulfate waters. *Rev. Mineral. Geochem.* **40**, 351–403.

Bigham J. M., Schwertmann U., Traina S. J., Winland R. L. and Wolf M. (1996) Schwertmannite and the chemical modeling of iron in acid sulfate waters. *Geochim. Cosmochim. Acta* **60**, 2111–2121.

Brady P. V. and House W. A. (1996) Surface-controlled dissolution and growth of minerals. In *Physics and Chemistry of Mineral Surfaces* (ed. P. V. Brady). CRC Press, Inc, Boca Raton, FL, pp. 225–305.

Brantley S. L. (2008) Kinetics of mineral dissolution. In *Kinetics of Water–Rock Interaction* (eds. S. L. Brantley, J. D. Kubicki and A. F. White). Spring Science+Business Media, LLC, New York, NY, pp. 151–210.

Carlson L., Bigham J. M., Schwertmann U., Kyek A. and Wagner F. (2002) Scavenging of As from acid mine drainage by schwertmannite and ferrihydrite: a comparison with synthetic analogues. *Environ. Sci. Technol.* **36**, 1712–1719.

Cheng H., Hu Y., Luo J., Xu B. and Zhao J. (2009) Geochemical processes controlling fate and transport of arsenic in acid mine drainage (AMD) and natural systems. *J. Hazard. Mater.* **165**, 13–26.

Driscoll R. and Leinze R. (2005) Methods for synthesis of some jarosites: U.S. Geological Survey Techniques and Methods 05–D1, p. 6.

Dutrizac J. E. and Jambor J. L. (2000) Jarosites and their application to hydrometallurgy. In: *Sulfate Minerals-Crystallography, Geochemistry, and Environmental Significance* (eds C. N. Alpers, J. L. Jambor, and D. K. Nordstrom). *Rev. Mineral. Geochem.* Mineralogical Society of America and Geochemical Society, Washington, D.C, vol. 40, pp. 405–452.

Eick M. J., Peak J. D. and Brady W. D. (1999) Effect of oxyanions on the oxalate-promoted dissolution of goethite. *Soil Sci. Soc. Am. J.* **63**(5), 1133–1141.

Elwood Madden M. E., Madden A. S. and Rimstidt J. D. (2009) How long was Meridiani Planum wet? Applying a jarosite stopwatch to constrain the duration of diagenesis. *Geology* **37**, 635–638.

Elwood Madden M. E., Madden A. S., Rimstidt J. D., Zahrai S., Kendall M. R. and Miller M. A. (2012) Jarosite dissolution rates and nanoscale mineralogy. *Geochim. Cosmochim. Acta* **91**, 306–321.

Emmet P. H. and Brunauer S. (1937) The use of low temperature van der Waals adsorption isotherms in determining the surface area of iron synthetic ammonia catalysts. *J. Am. Chem. Soc.* **59**, 1553–1564.

Fendorf S., Eick M. J., Grossl P. and Sparks D. L. (1997) Arsenate and chromate retention mechanisms on goethite. 1. Surface structure. *Environ. Sci. Technol.* **31**, 316–320.

Fuess H., Kratz T., Töpel-Schadt J. and Miehe G. (1987) Crystal structure refinement and electron microscopy of arsenopyrite. *Zeits. Krist.* **179**, 335–346.

Fukushi K. and Sverjensky D. A. (2007) A predictive model (ETLM) for arsenate adsorption and surface speciation on oxides consistent with spectroscopic and theoretical molecular evidence. *Geochim. Cosmochim. Acta* **71**, 3717–3745.

Fulignati P., Sbrana A., Luperini W. and Greco V. (2002) Formation of rock coatings induced by the acid fumaroles plume of the passively degassing volcano of La Fossa (Vulcano Island, Italy). *J. Vol. Geotherm. Res.* **115**, 397–410.

Galvez N., Barron V. and Torrent J. (1999) Effect of phosphate on the crystallization of hematite, goethite, and lepidocrocite from ferrihydrite. *Clay Clay Miner.* **47**, 304–311.

Gasharova B., Gottlicher J. and Becker U. (2005) Dissolution at the surface of jarosite: an in-situ AFM study. *Chem. Geol.* **215**, 499–516.

Hawthorne F. C., Krivovichev S. V. and Burns P. C. (2000) The crystal chemistry of sulphate minerals. In: *Sulfate Minerals-*

Crystallography, Geochemistry, and Environmental Significance (eds. C. N. Alpers, J. L. Jambor, and D. K. Nordstrom). *Rev. Mineral. Geochem.* Mineralogical Society of America and Geochemical Society, Washington, D.C, vol. 40, pp. 1–112.

Hendricks S. B. (1937) The crystal structure of alunite and the jarosites. *Am. Mineral.* **22**, 773–784.

Hyashi H. (1994) Mineralogy and chemistry of jarosite and acid sulphate soils. *Nendo Kagaku* **34**, 118–124.

Jain A. and Loeppert R. H. (2000) Effect of competing anions on the adsorption of arsenate and arsenite by ferrihydrite. *J. Environ. Qual.* **29**, 1422–1430.

Jambor J. L. (1999) Nomenclature of the alunite supergroup. *Can. Mineral.* **37**, 1323–1341.

Janney D. E., Cowley J. M. and Buseck P. R. (2000) Transmission electron microscopy of synthetic 2- and 6-line ferrihydrite. *Clays Clay Miner.* **48**, 111–119.

Kubisz J. (1970) Studies on synthetic alkali-hydronium jarosite. I. Synthesis of jarosite and natrojarosite. *Mineral. Pol.* **1**, 47–57.

Mitchell D. R. G. (2008) DiffTools: electron diffraction software tools for DigitalMicrograph™. *Microsc. Res. Tech.* **71**, 588–593.

Morin G. and Calas G. (2006) Arsenic in soils, mine tailings, and former industrial sites. *Elements* **2**, 97–101.

Paktunc D. and Bruggemann K. (2010) Solubility of nanocrystalline scorodite and amorphous ferric arsenate: implications for stabilization of arsenic in mine wastes. *Appl. Geochem.* **25**, 674–683.

Paktunc D. and Dutrizac J. E. (2003) Characterization of arsenate-for-sulfate substitution in synthetic jarosite using X-ray diffraction and X-ray absorption spectroscopy. *Can. Mineral.* **41**, 905–919.

Parker R. L. (1954) Alunitic alteration at Marysvale, Utah. Ph. D. thesis, Columbia Univ.

Papike J., Karner J. and Shearer C. (2006) Comparative planetary mineralogy: implications of Martian and terrestrial jarosite. A crystal chemical perspective. *Geochim. Cosmochim. Acta* **70**, 1309–1321.

Raven K. P., Jain A. and Loeppert R. H. (1998) Arsenite and arsenate adsorption on ferrihydrite: kinetics, equilibrium, and adsorption envelopes. *Environ. Sci. Technol.* **32**, 344–349.

Rieder R., Gellert R., Anderson R. C., Bruckner J., Clark B. C., Dreibus G., Economou T., Klingelhöffer G., Lugmair G. W., Ming D. W., Squyres S. W., d'Uston C., Wanke H., Yen A. and Zipfel J. (2004) Chemistry of rocks and soils at Meridiani Planum from the alpha particle X-ray spectrometer. *Science* **306**, 1746–1749.

Rimstidt J. D. and Newcomb W. D. (1993) Measurement and analysis of rate data: the rate of reaction of ferric iron with pyrite. *Geochim. Cosmochim. Acta* **57**, 1919–1934.

Ripmeester J. A., Ratcliffe C. I., Dutrizac J. E. and Jambor J. L. (1986) Hydronium in the alunite–jarosite group. *Can. Mineral.* **22**, 773–784.

Rustad J. R. and Casey W. H. (2012) Metastable structures and isotope exchange reactions in polyoxometalate ions provide a molecular view of oxide dissolution. *Nat. Mater.* **11**, 223–226.

Sapieszko R. S., Patel R. C. and Matijevic E. (1977) Ferric hydrous oxide sols. 2. Thermodynamics of aqueous hydroxo and sulfato ferric complexes. *J. Phys. Chem.* **81**, 1061–1068.

Savage K., Tingle T., O'Day P., Waychunas G. and Bird D. (2000) Arsenic speciation in pyrite and secondary weathering phases, Mother Lode Gold District, Tuolumne County, California. *Appl. Geol.* **15**, 1219–1244.

Savage K., Bird D. and O'Day P. (2005) Arsenic speciation in synthetic jarosite. *Chem. Geol.* **215**, 473–498.

Slowey A., Johnson S., Newville M. and Brown G. (2007) Speciation and colloid transport of arsenic from mine tailings. *Appl. Geochem.* **22**, 1884–1898.

Smith A., Dubbin W., Wright K. and Hudson-Edwards K. (2006a) Dissolution of lead- and lead–arsenic–jarosites at pH 2 and 8 and 20 °C: insights from batch experiments. *Chem. Geol.* **229**, 344–361.

Smith A., Hudson-Edwards K., Dubbin W. and Wright K. (2006b) Dissolution of jarosite $[KFe_3(SO_4)_2(OH)_6]$ at pH 2 and 8: insights from batch experiments and computational modeling. *Geochim. Cosmochim. Acta* **70**, 608–621.

Squyres S. W. et al. (2004) In situ evidence for an ancient aqueous environment at Meridiani Planum, Mars. *Science* **306**, 1709–1714.

Strauss R., Brümmer G. W. and Barrow N. J. (1997) Effects of crystallinity of goethite: II. Rates of sorption and desorption of phosphate. *Eur. J. Soil Sci.* **48**, 101–114.

Stumm W. (1997) Reactivity at the mineral–water interface: dissolution and inhibition. *Colloid Surf. A* **120**, 143–166.

Violante A., del Gaudio S., Pigna M., Ricciardella M. and Banerjee D. (2007) Coprecipitation of arsenate with metal oxides. 2. Nature, mineralogy, and reactivity of iron(III) precipitates. *Environ. Sci. Technol.* **41**, 8275–8280.

Waychunas G. A., Rea B. A., Fuller C. C. and Davis J. A. (1993) Surface chemistry of ferrihydrite: part 1. EXAFS studies of the geometry of coprecipitated and adsorbed arsenate. *Geochim. Cosmochim. Acta* **57**, 2251–2269.

Welch S. A., Christy A. G., Kirste D., Beavis S. G. and Beavis F. (2007) Jarosite dissolution I – trace cation flux in acid sulfate soils. *Chem. Geol.* **245**, 183–197.

Welch S. A., Kirste D., Christy A. G., Beavis F. and Beavis S. G. (2008) Jarosite dissolution II – reaction kinetics, stoichiometry and acid flux. *Chem. Geol.* **254**, 73–86.

Associate editor: Jacques Schott